

Inertial waves driven by differential rotation in a planetary geometry

DOUGLAS H. KELLEY[†], SANTIAGO ANDRÉS TRIANA[†],
DANIEL S. ZIMMERMAN[†], ANDREAS TILGNER[‡] and
DANIEL P. LATHROP^{*§}

[†]Department of Physics and Institute for Research in Electronics and Applied Physics,
University of Maryland, College Park, MD, 20742, USA

[‡]Institute of Geophysics, University of Göttingen, Friedrich-Hund-Platz 1,
D-37077 Göttingen, Germany

[§]Department of Physics, and Department of Geology,
Institute for Research in Electronics and Applied Physics,
Institute for Physical Science and Technology,
University of Maryland, College Park, MD, 20742, USA

(Received 30 November 2006; in final form 12 June 2007)

Dynamics occurring in the Earth's outer core involve convection, dynamo action, geomagnetic reversals, and the effects of rapid rotation, among other processes. Inertial waves are known to arise in rotating fluids, and their presence in the core has been previously argued using seismological data (Aldridge and Lumb 1987). They may also be involved in flows affecting the geodynamo. We report experimental observations of inertial wave modes in an Earth-like geometry: laboratory spherical Couette flow with an aspect ratio 0.33, using liquid sodium as the working fluid. Inertial modes are detected via magnetic induction and show good agreement with theoretical predictions in frequency, wavenumber, and magnetic induction structure. Our findings imply that linear wave behavior can dominate the dynamics even in turbulent flows with large Reynolds number Re , where nonlinear behaviors might be expected (here $Re \sim 10^7$). We present evidence that strong differential rotation excites the modes via over-reflection. Earth's inner core may also super-rotate and thereby excite inertial modes in the same way. Zonal flows in the core, likely to have higher speeds than the super-rotation, may be a stronger source for exciting inertial modes in the Earth.

Keywords: Inertial waves; Inertial modes; Spherical Couette flow; Electromagnetic induction; Turbulence; Over-rotation

1. Introduction

Inertial waves are Coriolis-restored motions often found in rotating fluids. According to at least one seismological study (Aldridge and Lumb 1987), inertial waves may be present in the liquid outer core of the Earth as well (though later work by Banka and

*Corresponding author. Email: dpl@complex.umd.edu

Crossley (1999) found the data used has a higher noise level than originally thought). Theoretical and experimental studies of inertial waves in the geophysics and fluid dynamics communities date back at least another century, to the work of Bryan (1889). A thorough treatment is given in the monograph of Greenspan (1969). Analytical solutions for the inertial wave equation in Earth-like (spherical shell) geometry are not known, but in the full, liquid sphere they do exist. One set of solutions was derived in the dissertation work of Kudlick (1966); a form more convenient for use in numerical calculations were found by Zhang *et al.* (2001). By performing experimental and numerical comparisons to these analytical solutions, Aldridge (1972) found that many of the inertial wave modes admitted by spherical shells have frequencies differing from their spherical counterparts by only a few percent. Zhang (1992) reinforced the findings by showing analytically that the structure and frequency of inertial waves with large azimuthal wavenumber are affected very little by the presence of an inner sphere. Numerical studies of rotating spherical shells in more recent years have proved fruitful, leading to the observation and description of ray behavior of the waves by Rieutord and Valdettaro (1997) and of attractors that can arise at certain frequencies by Tilgner (1999) and later Rieutord *et al.* (2001). Experimental work by Noir *et al.* (2001) and Lacaze *et al.* (2004), among others, has found inertial wave phenomena geometries. Hide and Stewartson (1972), Olson (1981), and Hide (1982) have suggested that inertial waves may contribute to dynamo action in the outer core of the Earth.

2. Equations of motion

2.1 Dynamics of the fluid

The Navier-Stokes equation, with terms accounting for steady rotation and for Lorentz forces, is

$$\frac{\partial \mathbf{u}}{\partial t} + (\mathbf{u} \cdot \nabla) \mathbf{u} + 2\boldsymbol{\Omega} \times \mathbf{u} = \nu \nabla^2 \mathbf{u} - \frac{1}{\rho} \nabla P + \frac{1}{\rho \mu_0} (\nabla \times \mathbf{B}) \times \mathbf{B} \quad (1)$$

in a frame of reference rotating at speed $\boldsymbol{\Omega} = \Omega \hat{\mathbf{z}}$, where \mathbf{u} is the fluid velocity field, t is the time, ν is the kinematic viscosity of the fluid, ρ is the density of the fluid, P is the generalized pressure (which includes centripetal acceleration), and \mathbf{B} is the magnetic field. Hats signify unit vectors. The last term on the left-hand side accounts for Coriolis acceleration. The last term on the right-hand side accounts for Lorentz forces.

Following Landau and Lifshitz (2004), we consider the case where $|\mathbf{B}|$ is small ($|\mathbf{B}|/l\eta\sqrt{\rho\mu_0} \ll 1$) and Ω is large ($\nu/2\Omega l^2 \ll 1$). Then the Coriolis term dominates (1) so that the nonlinear term (second on the left-hand side), the viscous damping term (first on the right-hand side), and the magnetic forcing term can all be neglected. With this linear and inviscid approximation, we take the curl of the resulting equation to eliminate the pressure term and obtain

$$\frac{\partial}{\partial t} \nabla \times \mathbf{u} = 2(\boldsymbol{\Omega} \cdot \nabla) \mathbf{u}. \quad (2)$$

Here $\nabla \times \mathbf{u}$ is the vorticity of the flow. Equation 2 admits wave solutions for \mathbf{u} of the form

$$\mathbf{u} = \tilde{\mathbf{u}} \exp i(\mathbf{k} \cdot \mathbf{x} + \omega t) \quad (3)$$

provided that the waves are transverse ($\tilde{\mathbf{u}} \cdot \mathbf{k} = 0$) and that they obey the peculiar dispersion relation

$$\omega = 2\hat{\mathbf{k}} \cdot \boldsymbol{\Omega}. \quad (4)$$

In these expressions $\tilde{\mathbf{u}}$ is a vector constant, $\hat{\mathbf{k}}$ is the unit wave vector, \mathbf{x} is the position vector, and ω is the frequency in the rotating frame. Waves of this type are known as inertial waves.

If we consider only the azimuthal behavior of the waves, the velocity can be written

$$\mathbf{u} = \tilde{\mathbf{u}}_\phi \exp i(m\phi + \omega t), \quad (5)$$

where $\tilde{\mathbf{u}}_\phi = \tilde{\mathbf{u}}_\phi(s, z)$ is a vector accounting for the polar and radial flow, and m is the azimuthal wavenumber. (Here we adopt cylindrical coordinates (s, ϕ, z) .) Hence in the rotating frame, the waves propagate in the azimuthal direction with angular velocity ω/m . Note that the form of (5) is such that $\omega > 0$ implies retrograde (westward) waves, i.e., waves propagating opposite the direction of bulk rotation. Changing to the laboratory frame, we require $\phi \rightarrow \phi' = \phi + \Omega t$, so that in the laboratory frame the observed frequency of the propagating pattern is

$$\omega_{\text{lab}} = m\Omega + \omega. \quad (6)$$

Further details of the behavior of the inertial waves depend, of course, on the boundary conditions imposed. In some geometries, inertial disturbances are possible at any frequency (a continuous spectrum). In other geometries, such as a spherical container, only certain frequencies are possible (a discrete spectrum), and inertial *modes* are said to be present. We identify the whole-sphere modes using azimuthal wavenumber m , polar wavenumber l , and dimensionless frequency ω/Ω . Our nomenclature is similar to that of Greenspan (1969), who used azimuthal wavenumber, polar wavenumber, and an ordinal corresponding to the frequency. Expressions for calculating \mathbf{u} when ω/Ω , m , and l are known can be found in the work of Greenspan (1969), Kudlick (1966), or Zhang *et al.* (2001).

2.2 Dynamics of the magnetic field

Analogous to the Navier-Stokes equation (1) that governs fluid motion is the induction equation, which governs the magnetic field:

$$\frac{\partial \mathbf{B}}{\partial t} = \eta \nabla^2 \mathbf{B} + \nabla \times (\mathbf{u} \times \mathbf{B}) \quad (7)$$

where η is the magnetic diffusivity of the fluid. We consider the case where a constant, external magnetic field $\mathbf{B}_0 = B_0 \hat{\mathbf{z}}$ is applied to the fluid. The total magnetic field, then, is the sum of this external field and an induced field: $\mathbf{B} = \mathbf{B}_0 + \mathbf{B}'$. In the case where

$|\mathbf{B}_0| \gg |\mathbf{B}'|$, application of a vector identity shows that the flow field \mathbf{u} produces a magnetic response according to

$$\frac{\partial \mathbf{B}'}{\partial t} = (\mathbf{B}_0 \cdot \nabla) \mathbf{u} + \eta \nabla^2 \mathbf{B}', \quad (8)$$

where small terms have been neglected. Thus, the magnetic induction can be used as a passive probe for the flow field under the condition $|B_0| \gg |B'|$. One may simply perform a direct integration that yields \mathbf{u} as long as \mathbf{B}_0 and \mathbf{B}' are known.

Even before performing such an integration, however, much can be said about the structure of \mathbf{u} . Bullard and Gellman (1954) developed useful selection rules for magnetic induction based on the azimuthal and polar wavenumbers of the three quantities \mathbf{u} , \mathbf{B}_0 , and \mathbf{B}' . With an external magnetic field $\mathbf{B}_0 = B_0 \hat{\mathbf{z}}$ as considered above, which has azimuthal and polar wavenumbers 0 and 1, respectively, we have a particularly simple special case of those selection rules: Both \mathbf{u} and \mathbf{B}' must have the same azimuthal wavenumber, and the polar wavenumbers must satisfy

$$|l - l_{mag}| = 1, \quad (9)$$

where l_{mag} is the polar wavenumber of \mathbf{B}' .

3. The experiment

Our experimental apparatus, sketched in figure 1, is a spherical Couette cell comprised of two independently rotating concentric spheres, diameters 20 and 60 cm, with liquid sodium filling the gap between them. The outer sphere has a titanium (alloyed with 6% Al and 4% V) wall 2.54 cm thick, and during experiments has been driven to various rotation rates $2.5 \text{ Hz} < \Omega_o/2\pi < 37 \text{ Hz}$. The inner sphere, machined from solid, high-conductivity copper, is rigidly mounted on a rotating inner shaft (304 stainless steel, 25 mm in diameter) and has been driven to various rotation rates between $-45 \text{ Hz} < \Omega_i/2\pi < 45 \text{ Hz}$, where $\Omega_i < 0$ denotes rotation in the direction opposite Ω_o . Very low rotation rates $|\Omega_i|/2\pi < 2.5 \text{ Hz}$ are inaccessible because of the limitations of our AC motor. The cavity between the two spheres is filled with about 110 L of sodium. Thermal control of the fluid is maintained by an array of 20 radiative heaters, each 0.5 kW, mounted near the lower hemisphere of the experiment. The temperature of the sodium, measured by an internal thermocouple mounted on the shaft near the inner sphere, is typically held between 100 and 110°C during experiments. The electrical resistivities of the titanium shell, the copper sphere, and the liquid sodium are $5.54 \times 10^{-5} \Omega \text{ m}$, $1.78 \times 10^{-6} \Omega \text{ m}$, and $4.1 \times 10^{-6} \Omega \text{ m}$, respectively. A DC magnetic field parallel to the rotation axis, with magnitude up to 0.04 T, is applied by a pair of external electromagnets, mounted near the poles of the outer sphere. Hence our parameter space has three dimensions: the applied magnetic field \mathbf{B}_0 , the outer sphere rotation rate Ω_o , and the inner sphere rotation rate Ω_i .

We measure the three control parameters as well as the temperature of the sodium and the rotational torque produced by the motors. The majority of the data, however, comes from Hall probes mounted in the non-rotating frame near the experiment. One probe (Ohio Semitronics HR72) is mounted near the bottom pole and oriented along

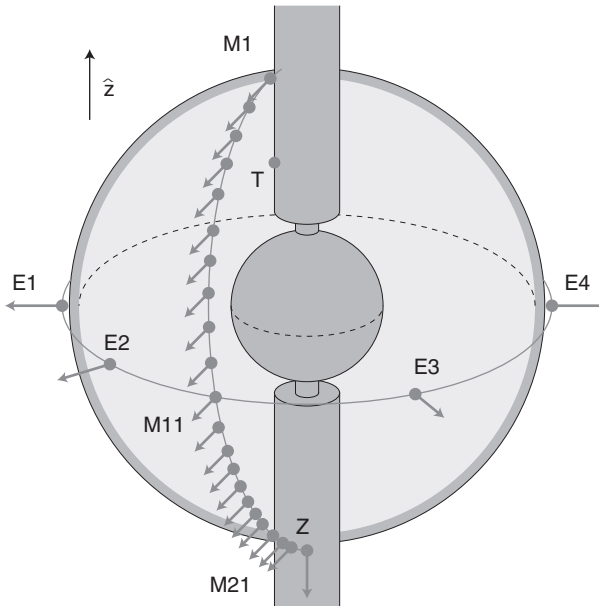


Figure 1. Diagram of the experimental setup. T marks the thermocouple; Z marks the Hall probe for measuring B_z ; labels beginning with E mark the equatorial Hall probes; and labels beginning with M mark the meridional Hall probes. The arrow at each Hall probe indicates the direction of its sensitivity. The shell between the inner and outer spheres is filled with sodium. An external field B_0 , oriented in the \hat{z} direction, is applied by two magnet coils, not shown.

the rotation axis to measure $B_z \equiv \mathbf{B} \cdot \hat{z}$. Four probes (also HR72) are mounted around the equator ($\phi \in [-90^\circ, -45^\circ, 45^\circ, 90^\circ]$) and oriented to measure $B_s \equiv \mathbf{B} \cdot \hat{s}$. Twenty-one probes (Honeywell SS94A1F) are mounted along the $\phi = 0$ meridian, spaced in equal increments of $\Delta\theta = 8.5^\circ$ in latitude, also oriented to measure B_s . The equatorial and meridional probes are oriented to exclude the external, axial magnetic field as much as possible. The error in their orientation is not more than a few degrees, based on field measurements during magnetic pulses. All HR72 probes have external amplifiers with adjustable gain allowing for sensitivities of 140 mV/G, 14 mV/G, or 1.4 mV/G. HR72 probes are mounted on liquid-cooled, copper heat sinks to reduce temperature fluctuations. SS94A1F probes have on-board amplifiers that give 25 mV/G sensitivity, as well as on-board temperature compensation circuits which limit temperature shift to less than 0.02%/°C. Each magnetic probe is sampled periodically at rates $f_s \sim 1$ kHz.

4. Results

Our basic observations are time traces of the magnetic field. Figure 2 shows measurements at the equator of $|\mathbf{B}_s| = |\mathbf{B}'_s|$, which is induced by fluid motions interacting with the external magnetic field (without which the magnetic induction is negligible). Power spectra of the same data are shown in figure 3. At many parameter combinations, and in particular at the parameter combinations shown in in figures 2 and 3, striking oscillations are present. Since the power scale in each spectral plot is

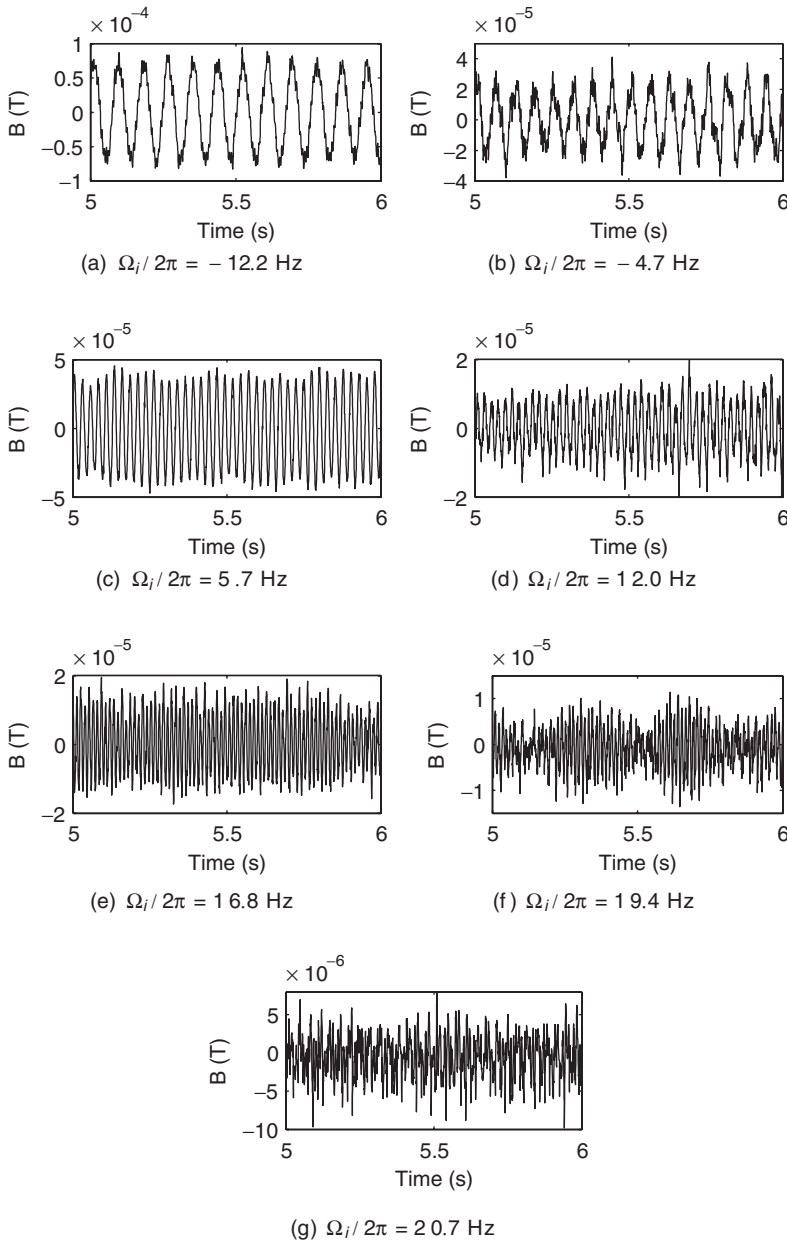


Figure 2. Typical B_s time traces at an equatorial probe. Only the oscillating component is shown, i.e., the means have been removed. For all data shown here, $\Omega_o/2\pi = 29.9$ Hz and $B_0 = 0.015$ T.

logarithmic, the strongest frequencies plotted have power levels two or three orders of magnitude above the noise. The induced field depends strongly on the dimensionless rotation ratio $\chi \equiv \Omega_i/\Omega_o$, given with each plot. Also, the induced field varies linearly with the applied field, suggesting that the oscillations are due to hydrodynamic phenomena, not magnetohydrodynamic ones.

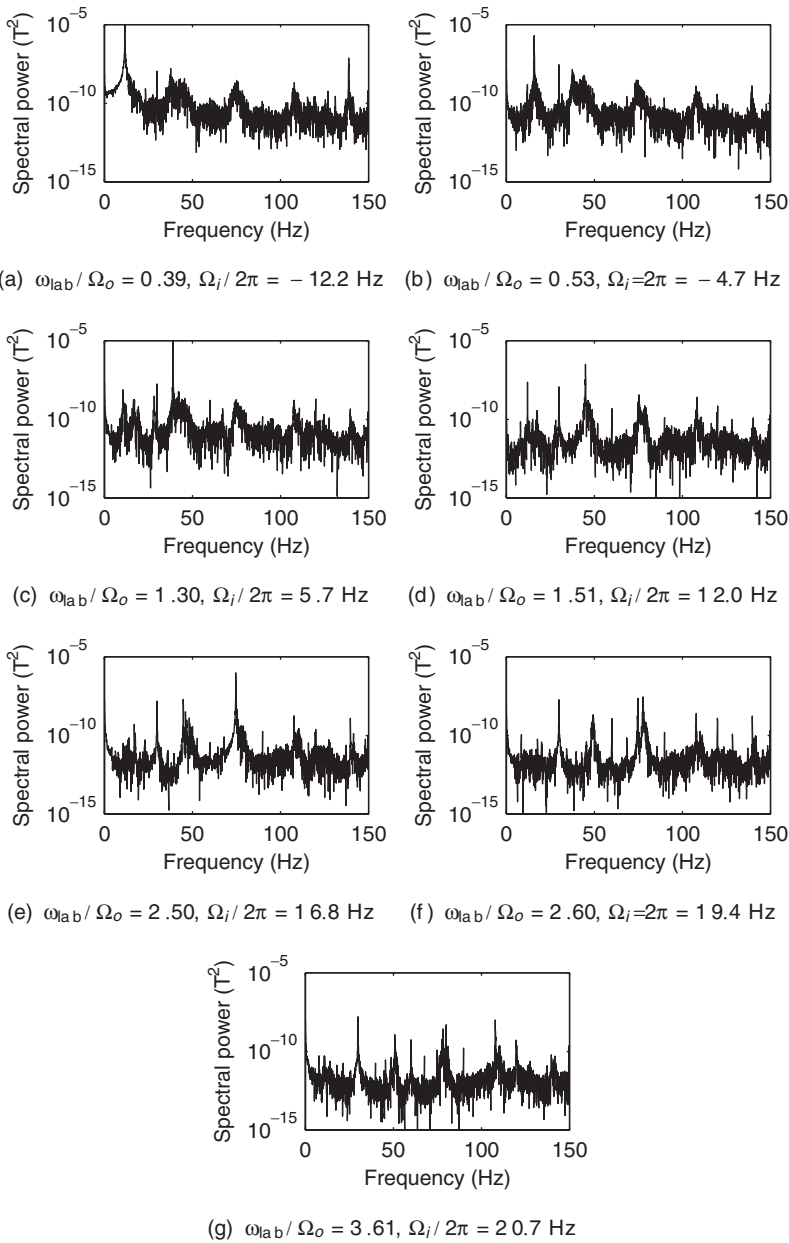


Figure 3. Power spectra of the time traces shown in figure 2. The dominant frequency in each signal is listed as $\omega_{\text{lab}} / \Omega_o$.

We seek to learn more about the oscillations noted in such time series. Using a collection of similar data sets taken from the same equatorial probe, we stack many sequential frequency spectra of the kind shown in figure 3, each at slightly different χ , to produce spectrograms of the type in figure 4. Each column of pixels represents one spectrum, produced from 15 or 16 s of data, with frequency now on the vertical axis and

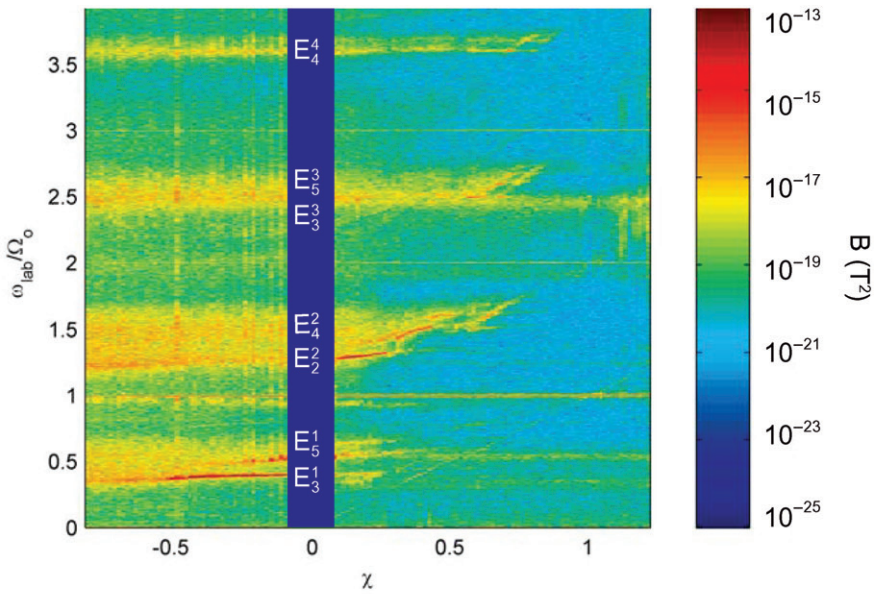
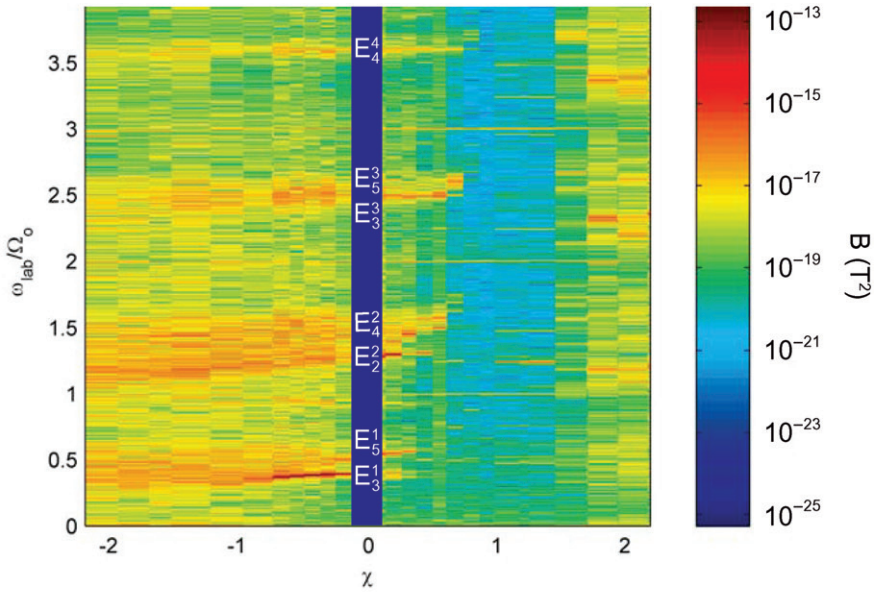
(a) $\Omega_o/2\pi = 29.9$ Hz(b) $\Omega_o/2\pi = 19.9$ Hz

Figure 4. Spectrograms of magnetic field data taken from an equatorial Hall probe. The vertical axis shows the normalized signal frequency $\omega_{\text{lab}}/\Omega_o$ as measured in the laboratory frame, and the horizontal axis shows the normalized rotation rate of the inner sphere χ . Each column of pixels is a Fourier transform of ~ 15 s of data. The color indicates spectral power. The blank central region lies at low speeds inaccessible with our AC motors. Strong modes are labeled with letters; see table 1. The two plots come from two different rotation rates of the outer sphere.

with spectral power, still logarithmic, now represented by color. A number of dominant frequency modes are immediately apparent. The modes are reproducible and change abruptly as we vary χ smoothly. Some hysteresis is observed; the data shown are taken for rising χ . When χ is falling, we observe most of the same modes, though some of their edges shift and some modes fail to appear. The horizontal line visible at $\omega_{\text{lab}}/\Omega_o = 1$ and its harmonics are present because our probes detect weak magnetic imperfections (bolts) spinning on the outer sphere itself. A similar, sloping line is sometimes visible and indicates the rotation rate of the inner sphere. Though our AC motors prevent us from spinning the inner sphere to achieve very small χ , we have performed experiments with the inner sphere fixed ($\chi = 0$), in which we observe the presence of the same mode seen in $\chi \approx 0$ experiments.

We emphasize here that the magnetic field \mathbf{B}_0 applied during these experiments remains steady; hence, the presence of oscillations in these signals is a clear sign of induction due to the fluid flow. From these plots alone we cannot say what flows are present, but the periodic oscillations detected are consistent with patterns stationary in some rotating frame. We shall proceed with this hypothesis and seek to determine whether or not the rotating patterns are in fact due to inertial modes. A positive identification would require matching our observations to theory via three quantities, as described in : the azimuthal wavenumber m , the polar wavenumber l , and the frequency ω .

4.1 Azimuthal wavenumber

In order to determine the azimuthal wavenumber m of each rotating pattern, we harness data from additional equatorial probes. As described in , inertial waves are patterns propagating with angular velocity ω/m . In the presence of such a pattern we would expect that two probes at the same latitude and separated by an angle $\Delta\phi$ would record signals $B_{s,1}(t)$ and $B_{s,2}(t)$ that are identical except for a time delay Δt . The correlation of the two signals is

$$C(\tau) = \frac{\langle B_{s,1}(t)B_{s,2}(t + \tau) \rangle}{\sigma_{B_{s,1}}\sigma_{B_{s,2}}}, \quad (10)$$

where $\langle \rangle$ signifies averaging over t and σ_X is the standard deviation of X . Since $C(\tau)$ has a maximum when $\tau = \Delta t$, we can use the correlation to calculate Δt . The azimuthal wavenumber is then

$$m = \frac{\omega\Delta t}{\Delta\phi}. \quad (11)$$

4.2 Polar wavenumber

Next we set out to determine the polar wavenumber l . A pattern with azimuthal wavenumber m completes one rotation in the period $2\pi m\omega_{\text{lab}}^{-1}$. For flow patterns stationary in some rotating frame, the range in time $0 < t < 2\pi m\omega_{\text{lab}}^{-1}$ can be mapped directly onto the range in azimuthal angle $0 < \phi < 2\pi$. Employing such a mapping

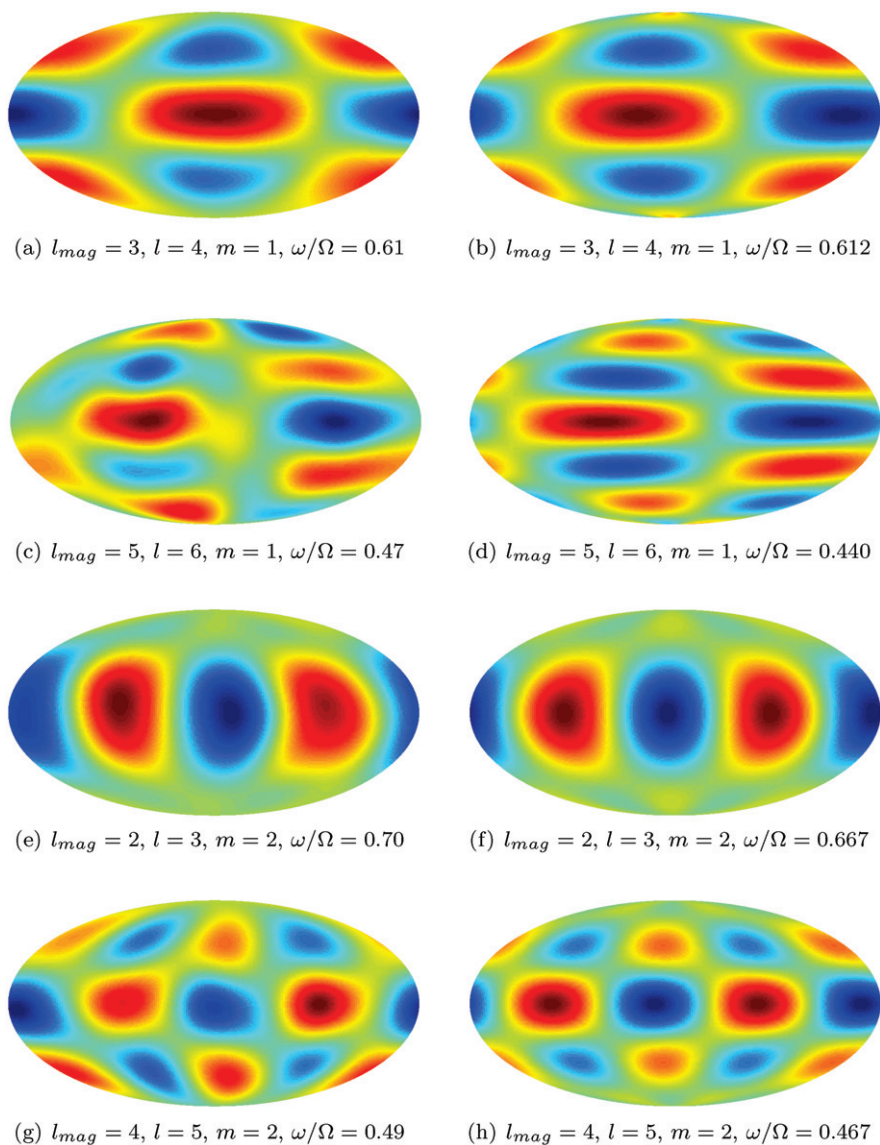


Figure 5. Induction B_s/B_0 over one revolution of the dominant pattern, shown as a Mollweide projection. Figures 5(a), 5(c), 5(e), and 5(g) show data taken under the same experimental conditions as figures 2(a), 2(b), 2(c), and 2(d), respectively. Figures 5(b), 5(d), 5(f), and 5(h) show results calculated in simulation.

allows us to use our array of 21 meridional probes in the laboratory frame to sample the pattern at various ϕ as it rotates past. We stack the 21 time series to construct a map (image) of the structure of the pattern over the surface of the outer sphere. Images of this type are shown on the left side of figures 5 and 6, one for each experimental condition listed in figure 2.

These images show patterns of magnetic induction that are oscillatory in both of the spherical coordinates ϕ and θ ; often the polar wavenumber of the induction, l_{mag} , can be

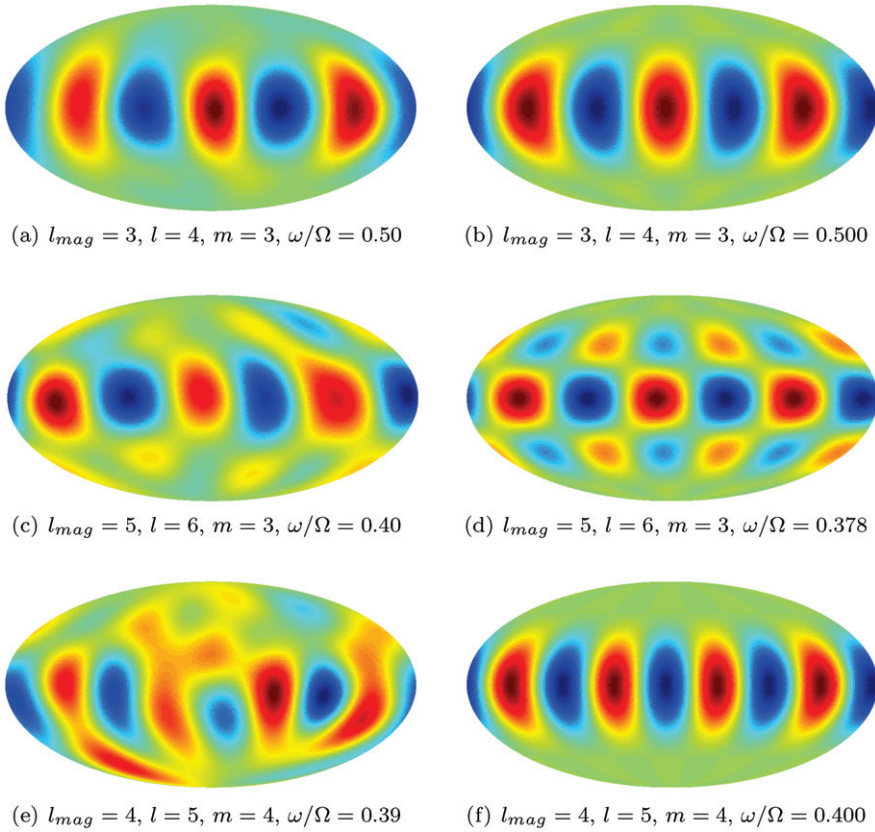


Figure 6. Induction B_s/B_0 over one revolution of the dominant pattern, shown as a Mollweide projection. Figures 6(a), 6(c), and 6(e) show data taken under the same experimental conditions as figures 2(e), 2(f), and 2(g), respectively. Figures 6(b), 6(d), and 6(f) show results calculated in simulation.

determined by eye. In the interest of rigor, we have projected the data onto the scalar spherical harmonics, one of which is dominant in all cases shown, thereby yielding a clear l_{mag} describing the induction pattern. (Note that figures 5 and 6 include harmonics only up to $l=12$.)

We now return to explain the labels in figure 4. All regular magnetic field patterns we have observed are even with respect to reflection across the equator, i.e., $B_s(\theta - \pi/2) = B_s(\pi/2 - \theta)$, so we label them “E.” Each subscript indicates the polar wavenumber l_{mag} of the mode, and each superscript represents the azimuthal wavenumber m .

4.3 Frequency

The last quantity necessary to identify an inertial mode is its frequency ω , which is related to ω_{lab} as measured in the laboratory frame according to (6). With the approximation that $\Omega = \Omega_o$ (to be discussed further below), we calculate ω/Ω_o for each mode shown above. Each mode shows a range of frequency because we find some

Table 1. Experimental and theoretical characteristics of inertial wave modes. In the last column we have included the nomenclature of Greenspan (1969).

| Label | Experiment | | | | Theory | | | |
|---------|------------|-----|-----|-------------------|--------|-----|-----------------|-----------|
| | l_{mag} | l | m | ω/Ω_o | l | m | ω/Ω | Greenspan |
| E_2^2 | 2 | 3 | 2 | 0.683–0.698 | 3 | 2 | 0.667 | (3,1,2) |
| E_3^1 | 3 | 4 | 1 | 0.602–0.627 | 4 | 1 | 0.612 | (4,3,1) |
| E_3^3 | 3 | 4 | 3 | 0.509–0.511 | 4 | 3 | 0.500 | (4,1,3) |
| E_4^2 | 4 | 5 | 2 | 0.492–0.531 | 5 | 2 | 0.467 | (5,3,2) |
| E_4^4 | 4 | 5 | 4 | 0.404–0.407 | 5 | 4 | 0.400 | (5,1,4) |
| E_5^1 | 5 | 6 | 1 | 0.435–0.450 | 6 | 1 | 0.440 | (6,5,1) |
| E_5^3 | 5 | 6 | 3 | 0.404–0.413 | 6 | 3 | 0.378 | (6,3,3) |

variation in ω through the course of our experiments. Notice, for instance, that the high-power bands in figure 4 are not strictly horizontal, but increase slightly in frequency as χ grows. Repeating the experiment reproduces the behavior in that we observe the same dependence of ω on χ .

4.4 Theory and simulation

Via the procedures outlined in sections 4.1–4.3, we have produced m , l_{mag} , and ω/Ω_o for each induction pattern shown in figure 2. We find that we can match our experimental data to specific modes of the full sphere (not the spherical shell, for which limited solutions are known) if $l = l_{mag} + 1$ in all cases. Note that the selection rule given in (9) is thus satisfied. The results are listed in table 1. Under the heading “Experiment” are our observed data; under the heading “Theory” are theoretical wavenumbers and frequencies for a few of the inertial modes possible in a sphere, calculated via the technique in Zhang *et al.* (2001). We have also included the nomenclature of Greenspan (1969) for clarity. Note that, since $\omega/\Omega_o > 0$ in all cases, these wave modes propagate in the retrograde (westward) direction.

For further comparison, we have produced numerical simulations of the same modes chosen in table 1, first finding the velocity field \mathbf{u} and subsequently using the induction equation (7) to determine B_s induced from \mathbf{B}_0 . The resulting field maps (images) are plotted on the right side of figures 5 and 6. Qualitatively, the agreement with our experimental data (on the left) is immediately apparent, leading to some confidence that the modes first plotted in figure 2 are indeed due to excited inertial modes in the sodium flow.

4.5 Flow fields

We return now to the notion of using the magnetic induction as a probe for the flow field. Liquid sodium is opaque and therefore incompatible with common imaging techniques. Ultrasound doppler velocimetry has been developed (Takeda 1991) and has been utilized in various settings (Noir *et al.* 2001, Sisan *et al.* 2004, Brawn *et al.* 2005), but each ultrasound probe can measure only one component of the velocity and only along one line in space. On the other hand, if we know that a particular inertial mode is present and have an analytical solution giving its flow field, we have good knowledge of

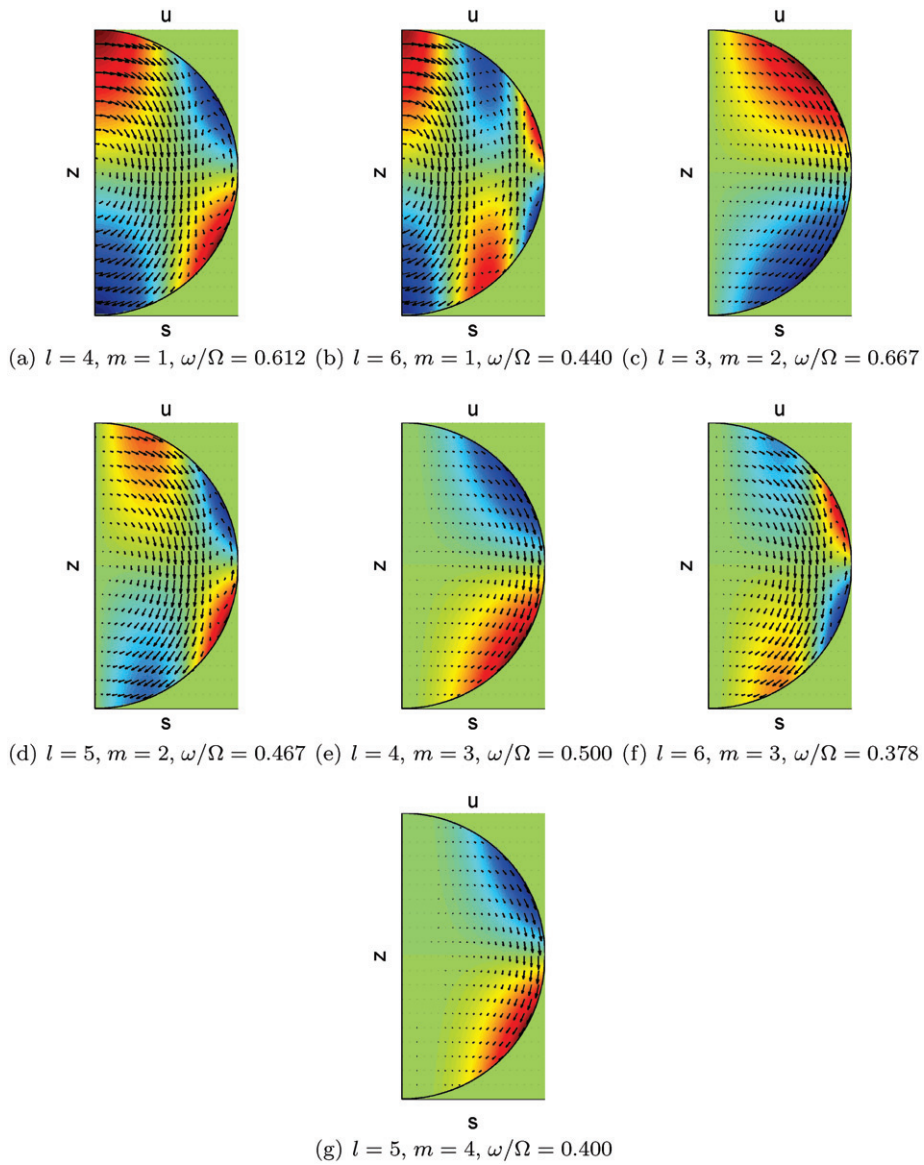


Figure 7. Velocity \mathbf{u} of the inertial modes that produce the induction shown in figures 5 and 6. Each diagram is a meridional plane in the bulk, with the axis of rotation at left and the radius normalized to 1. Arrows indicate the velocity components in the (s, z) plane and color indicates the velocity component in the ϕ direction, with red for prograde flow and blue for retrograde. These plots are meant to show shape only; amplitude scales are arbitrary.

the three-dimensional flow throughout the opaque liquid. Figure 7 shows plots of the velocity \mathbf{u} for each mode. Of course in a real-world apparatus, the motion due to the inertial mode will be combined to some extent with other, possibly turbulent, motions. However, plots like the frequency spectra shown in figure 3 gauge the strength of those other effects. If the frequencies associated with inertial modes have much more power

than other frequencies, as is the case for the experimental data considered here, the actual flows deviate little from motion due to the inertial mode. We estimate that in our data the deviation is perhaps a few percent, but not more in the range $-0.5 \leq \chi \leq 0.85$. We hope in future work to add ultrasound velocimetry probes to the experiment such that their measurements can be corroborated with the flow fields deduced here.

Above we mentioned that the magnetic induction observed in our experiments is always symmetric with respect to the equator. In agreement with (9), the corresponding velocity fields are anti-symmetric with respect to the equator, i.e.,

$$u_\phi(z) = -u_\phi(-z) \quad u_s(z) = -u_s(-z) \quad u_z(z) = u_z(-z). \quad (12)$$

In contrast, previous experiments (Aldridge and Toomre 1969), found modes with velocity fields symmetric with respect to the equator. This difference in symmetry, like mode selection and forcing (see below), remains an open question for further exploration.

5. Discussion

5.1 Forcing and energy input

Past researchers who observed inertial modes in an experimental apparatus have often introduced a perturbation tuned to the natural frequency of the mode of interest in order to transfer energy into that mode (Aldridge and Toomre 1969). Others have excited inertial modes via precession (Malkus 1968, Noir *et al.* 2001). Our situation is different—we are not directly exciting the system at the modal frequencies. Any inertial modes in the system must be excited somehow through the differential rotation of the outer and inner spheres or the resulting boundary layers.

To learn more about the excitation, we have examined the quality factor of each mode, defined as $Q = \omega_{\text{lab}} / \Delta\omega_{\text{lab}}$, where $\Delta\omega_{\text{lab}}$ is the half-width-half-max broadness of the resonant peak. We compare the quality factor to the relative strength of the mode, $B_{s,\text{peak}}/B_{s,\text{noise}}$. If $B_{s,\text{peak}}/B_{s,\text{noise}} \sim Q$, the observed inertial modes could plausibly be described as linear resonators excited by turbulent fluctuations; if $B_{s,\text{peak}}/B_{s,\text{noise}} \gg Q$, there must be a non-random amplification mechanism. Our results are listed in table 2. In all cases, $B_{s,\text{peak}}/B_{s,\text{noise}} \gg Q$, suggesting that these inertial modes arise as instabilities.

Thus, we seek a process by which energy might be transferred to the inertial modes. One such process is so-called over-reflection, as found by Ribner (1957). Consider two adjacent regions of fluid, one of which has a bulk velocity with respect to the other—a

Table 2. Quality factor and resonant strength of inertial wave modes.

| l | m | ω | $B_{s,\text{peak}}/B_{s,\text{noise}}$ | Q | $B_{s,\text{peak}}/B_{s,\text{noise}}/Q$ |
|-----|-----|----------|--|-----|--|
| 3 | 2 | 0.667 | 4200 | 59 | 90 |
| 4 | 1 | 0.612 | 5700 | 15 | 820 |
| 4 | 3 | 0.500 | 3500 | 51 | 68 |
| 5 | 2 | 0.467 | 780 | 51 | 17 |
| 6 | 1 | 0.440 | 2200 | 23 | 190 |

shear flow. The boundary between the two flows can reflect and refract fluid waves according to the usual relations

$$\frac{A_r}{A_i} = \frac{1 - Z}{1 + Z}, \quad \frac{A_t}{A_i} = \frac{2}{1 + Z}. \quad (13)$$

Here A_r is the amplitude of the reflected wave, A_i is the amplitude of the incoming wave, A_t is the amplitude of the transmitted wave, and Z is the impedance mismatch of the two regions. The waves, in turn, cause a ripple to form on the boundary. In the frame of reference in which this ripple is stationary, the region of fluid through which the incoming wave travels has some bulk velocity U_1 ; likewise the region through which the transmitted wave travels has some bulk velocity U_2 . With the the wave speed c , we can use these velocities to construct the Mach angles α_1 and α_2 , defined according to $\csc \alpha_1 = U_1/c$ and $\csc \alpha_2 = U_2/c$, respectively. Ribner shows that, provided $|U_1| \geq c$ and $|U_2| \geq c$, the impedance mismatch is governed by the Mach angles:

$$Z = \frac{\sin 2\alpha_2}{\sin 2\alpha_1} \quad (14)$$

For certain Mach angles, Z can be negative, implying over-reflection, i.e., $A_r > A_i$. Thus energy is transferred from the shear flow to the reflected wave. Equivalently, we may consider the frame of reference in which the region through which the incoming wave travels is stationary. In this frame, defining the Mach number of the other region as $M'_1 = (U_1 - U_2)/c$, over-reflection is possible when $M'_1 > 2$.

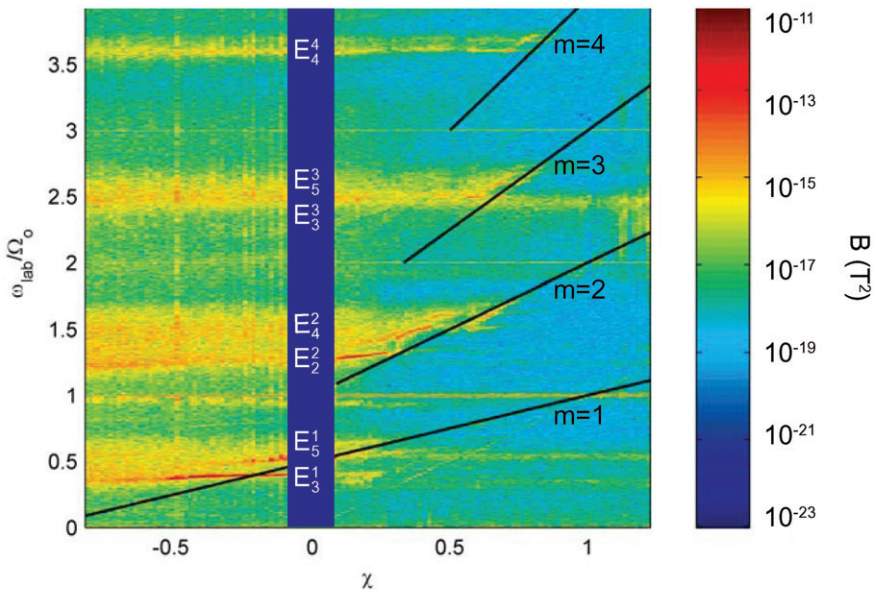
The differential rotation of the outer and inner boundaries of our experiment imparts shear upon the fluid. Most likely that shear is localized to (possibly turbulent) Ekman layers near the boundaries and a Stewartson layer near the tangent cylinder. We postulate that at one of these shear layers, the interior region of fluid is rotating near Ω_i , while the exterior region is rotating near Ω_o . In the rotating frame of the exterior region, the velocity of the surface of the interior region is $v = (\Omega_i - \Omega_o)r$, where r is the radius of the shear layer. Extracting the azimuthal wave speed from (5), the Mach number of the interior region becomes

$$M = \frac{m\Omega_o}{\omega}(\chi - 1). \quad (15)$$

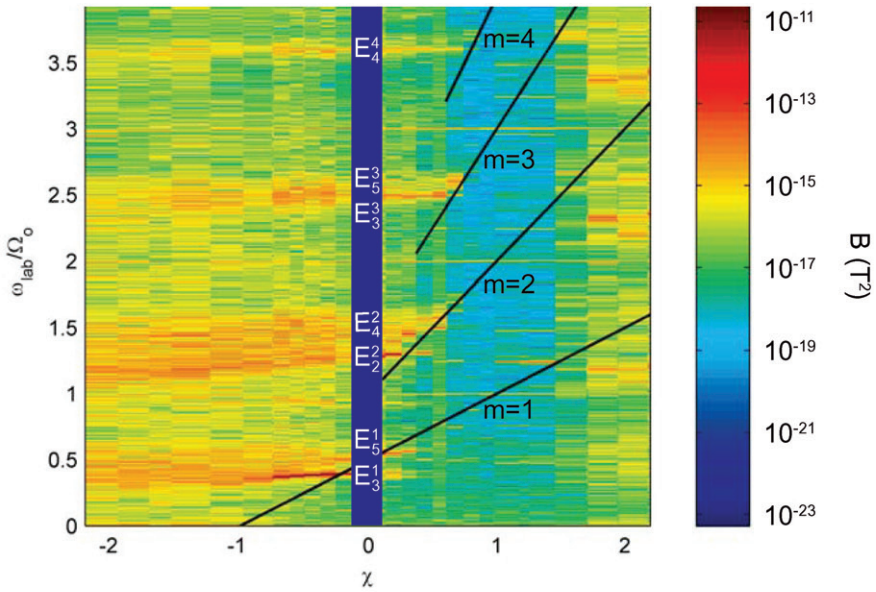
in the rotating frame. We now use (6) and solve for the frequency measured in the laboratory frame when the interior region has Mach number M with respect to the exterior:

$$\frac{\omega_{\text{lab}}}{\Omega_o} = \frac{m}{M}(\chi - 1 + M). \quad (16)$$

From the arguments above, over-reflection is possible when $M \geq 2$. We set $M = 2$ and plot (16) for various m in figure 8. On the same axes we show the spectrograms shown previously in figure 4. Inspection shows that the inertial wave modes listed in table 1 arise near $M = 2$. When $M < 2$, little induction of any kind is present. For $M \gg 2$, the narrowband modes weaken and are replaced by broadband signals over the frequency ranges where inertial waves are possible, as would be expected if many different inertial modes were excited. Hence we are led to believe that energy input to the inertial modes may come from over-reflection.



(a) $\Omega_o/2\pi = 29.9$ Hz



(b) $\Omega_o/2\pi = 19.9$ Hz

Figure 8. Spectrograms identical to those shown in figure 4, with $M=2$ lines included. Each value of the azimuthal wavenumber m has a different line, as indicated.

5.2 Mode selection

Having identified over-reflection as a likely mechanism for transfer of energy from the bulk flow to the inertial wave modes, one must consider selection mechanisms.

Table 3. Dimensionless parameters.

| Parameter | Experiment | Earth |
|-----------|-------------------|-------------|
| Re | 1.5×10^7 | 10^7-10^8 |
| Rm | 140 | 10-100 |
| Ro | 0.013 | 10^{-7} |

Analytically, the inertial modes of a sphere are infinite in number and dense in ω . Our experiments repeatably produce just a few of the modes; seven are listed in table 1. Being a local phenomenon, over-reflection must match the frequency and wavenumbers of whatever modes are otherwise present, and hence it imposes no obvious selection rules of its own.

For one clue to mode selection, we note that $M > 2$ is a necessary condition for over-reflection, but not a sufficient one, because the ripple speed is not necessarily equidistant from the two bulk flow speeds. As Ribner writes, “there exists a certain angle of incidence at which the ripples move at just half the stream speed.” Moreover, M as calculated above gives the Mach number of the inner sphere at its equator, and pumping of modes must first occur at the equator. Perhaps careful consideration of the geometry of the problem will lead to clear selection rules. Finally, we note that each observed inertial mode has the lowest possible positive frequency ω for its given wavenumbers l and m . Perhaps this fact, too, can serve as a clue to mode selection in future work.

5.3 Implications for Earth

In order to consider possible implications of our findings for the Earth, we introduce a few additional dimensionless parameters. Both our experiment and the Earth can be characterized by a Reynolds number Re , a magnetic Reynolds number Rm , and a Rossby number Ro :

$$Re \equiv \frac{UL}{\nu} \quad Rm \equiv \frac{UL}{\eta} \quad Ro \equiv \frac{U_r}{\Omega L}. \tag{17}$$

Here U is a characteristic velocity, L is a characteristic length, and U_r is a characteristic velocity in the rotating frame. Table 3 compares the dimensionless parameters of our experiment to those of the Earth. To calculate the experimental values shown, we used $\nu = 7.39 \times 10^{-7} \text{ m}^2/\text{s}$ and $\eta = 0.083 \text{ m}^2/\text{s}$ for sodium at our typical operating temperatures. Also we have chosen $L = 20 \text{ cm}$, $U = 2\pi \times 30 \text{ Hz} \times 30 \text{ cm}$, and $U_r = 0.5 \text{ m/s}$. Thus L is the width of the gap between the inner and outer spheres, U is the tangential velocity of the outer sphere, and U_r is an estimate of the fluid velocity in the rotating frame when inertial modes are present. To arrive at this value for U_r , we have used the fact that \mathbf{B}' is a linear function of \mathbf{u} in the regime of interest, so that

$$U_r = |\mathbf{B}'|_{\text{experiment}} \frac{|\mathbf{u}|_{\text{simulation}}}{|\mathbf{B}'|_{\text{simulation}}}. \tag{18}$$

Values for the parameters of the Earth are taken from Cardin and Olson (1994).

We note that spherical Couette flows become unstable and turbulent at Reynolds numbers significantly lower than the ones explored in these experiments. Thus one might expect nonlinear motions to dominate the dynamics, but we have found that in these parameter regimes, linear wave motions are dominant.

In terms of these dimensionless numbers, our system is in a parameter regime similar to that of the Earth. The greatest discrepancy, the Rossby number, does not arouse our concern for the following reason: Assuming that Ω is large in order to arrive at (2) is equivalent to assuming that $Ro \ll 1$, so that the approximation is even better for the Earth than for our experiment. Our system differs starkly from the Earth in its lack of density contrast, however. The two systems also differ in their forcing. The inertial modes we have identified above result when the inner sphere has retrograde motion, sometimes even rotating in the opposite direction as the outer sphere. In contrast, the inner core of the Earth is suspected to show only very slight differential rotation, and that motion is prograde—a super-rotation of about 1° per year at most (Song and Richards 1996). Can the modes we have identified say anything about the Earth?

We note that some induction does occur in our experiment for prograde rotation (see figure 4(b)), though we have not focused on that region of parameter space. The induction observed obeys $M > 2$ and may be inertial modes. It is possible to use (15) with the known rate of super-rotation of Earth's core to predict the minimum m possible via over-reflection in the core. Assuming $\omega/\Omega_o \sim 1$ yields $m \sim 10^5$, implying waves features with a characteristic size on the order of 100 m. Modes with $\omega/\Omega_o \ll 1$ might arise with smaller m and larger characteristic size.

Ekman layers and a Stewartson layer are not the only possible shear layers in the core of the Earth, however. Experiment and theory suggest that zonal flow, i.e., a bulk azimuthal drift, may play a significant role. The westward drift of Earth's magnetic field (Bullard *et al.* 1950) indicates a likely retrograde zonal flow. In the experimental realm, Cardin and Olson (1994) constructed a rotating spherical shell and cooled its inner sphere to induce Earth-like convection. They found that convection gave rise to zonal flow which became “ubiquitous when the convection is fully developed.” With numerics Aurnou *et al.* (1996) also found that convection can drive zonal flow. With sufficient speed, zonal flows in planetary cores might pump inertial modes via over-reflection, also yielding small-scale azimuthal wavenumbers.

6. Conclusion

We have experimentally detected inertial modes in Earth-like geometry using magnetic induction. Our data show good agreement in wavenumber, frequency, and structure with the behavior of inertial modes known to theory. The relationships among the wavenumbers of the flow, the external magnetic field, and the induced field obey appropriate selection rules from theory. The presence of wave motions is perhaps surprising in that they are linear phenomena occurring in flows that are highly turbulent ($Re \sim 10^7$). Some evidence suggests that the waves are forced by differential rotation of the inner sphere via over-reflection. However, selection rules governing which inertial modes arise via over-reflection, both in experiment and perhaps in planetary cores, remain an open and interesting question.

References

- Aldridge, K.D. and Lumb, I., Inertial waves identified in the earth's fluid outer core. *Nature*, 1987, 325, 421–423.
- Aldridge, K.D. and Toomre, A., Axisymmetric inertial oscillations of a fluid in a rotating spherical container. *J. Fluid Mech.*, 1969, 37, 307–323.
- Aldridge, K.D., Axisymmetric inertial oscillations of a fluid in a rotating spherical shell. *Mathematika*, 1972, 19, 163–168.
- Aurnou, J.M., Brito, D. and Olson, P.L., Mechanics of inner core superrotation. *Geophys. Res. Lett.*, 1996, 23, 3401–3404.
- Banka, D. and Crossley, D., Noise levels of superconducting gravimeters at seismic frequencies. *Geophys. J. Int.*, 1999, 139, 87–97.
- Brawn, B.E., Joshi, K., Lathrop, D.P., Mujica, N. and Sisan, D.R., Visualizing the invisible: ultrasound velocimetry in liquid sodium. *Chaos*, 2005, 15, 041104. DOI: 10.1063/1.2126811.
- Bryan, G.H., The waves on a rotating liquid spheroid of finite ellipticity. *Philos. T. R. Soc. A*, 1889, 180, 187–219.
- Bullard, E., Freedman, C., Gellman, H. and Nixon, J., The westward drift of the earth's magnetic field. *Philos. T. R. Soc. A*, 1950, 243, 67–92.
- Bullard, E. and Gellman, H., Homogeneous dynamos and terrestrial magnetism. *Philos. T. R. Soc. A*, 1954, 247, 213–278.
- Cardin, P. and Olson, P.L., Chaotic thermal convection in a rapidly rotating spherical shell: consequences for flow in the outer core. *Phys. Earth Planet. In.*, 1994, 82, 235–239.
- Greenspan, H.P., *The Theory of Rotating Fluids*. Cambridge Monographs on Mechanics and Applied Mathematics. 1969 (Cambridge University Press, London).
- Hide, R., On the role of rotation in the generation of magnetic fields by fluid motions. *Philos. T. R. Soc. A*, 1982, 306, 232–234.
- Hide, R. and Stewartson, K., Hydromagnetic oscillations of the earth's core. *Rev. Geophys. Space GE*, 1972, 10, 579–598.
- Kudlick, M.D., *On Transient Motions in a Contained, Rotating Fluid*. PhD thesis, Massachusetts Institute of Technology, 1966.
- Lacaze, L., Le Gal, P. and Le Dizes, S., Elliptical instability in a rotating spheroid. *J. Fluid Mech.*, 2004, 505, 1–22.
- Landau, L.D. and Lifshitz, E.M., *Fluid Mechanics*. Theoretical Physics. 2nd Edn. 2004 (Elsevier, Oxford, England).
- Malkus, W.V.R., Precession of the earth as the cause of geomagnetism. *Science*, 1968, 160, 259–264.
- Noir, J., Brito, D., Aldridge, K.D. and Cardin, P., Experimental evidence of inertial waves in a precessing spheroidal cavity. *Geophys. Res. Lett.*, 2001, 28, 3785–3788.
- Olson, P., A simple physical model for the terrestrial dynamo. *J. Geophys. Res.*, 1981, 86, 10875–10882.
- Ribner, H.S., Reflection, transmission, and amplification of sound by a moving medium. *J. Acoust. Soc. Am.*, 1957, 29, 435–441.
- Rieutord, M., Georgeot, B. and Valdetaro, L., Inertial waves in a rotating spherical shell: Attractors and asymptotic spectrum. *J. Fluid Mech.*, 2001, 435, 103–144.
- Rieutord, M. and Valdetaro, L., Inertial waves in a rotating spherical shell. *J. Fluid Mech.*, 1997, 341, 77–99.
- Sisan, D.R., Mujica, N., Tillotson, W.A., Huang, Y., Dorland, W., Hassam, A.B., Antonsen, T.M. and Lathrop, D.P., Experimental observation and characterization of the magnetorotational instability. *Phys. Rev. Lett.*, 2004, 93, 114502. DOI: 10.1103/PhysRevLett.93.114502.
- Song, X. and Richards, P.G., Seismological evidence for differential rotation of the earth's inner core. *Nature*, 1996, 382, 221–224.
- Takeda, Y., Development of an ultrasound velocity profile monitor. *Nucl. Eng. Des.*, 1991, 126, 277–284.
- Tilgner, A., Driven inertial oscillations in spherical shells. *Phys. Rev. E*, 1999, 59, 1789–1794.
- Zhang, K., On inertial waves in the earth's fluid core. *Geophys. Res. Lett.*, 1992, 19, 737–740.
- Zhang, K., Earnshaw, P., Liao, X. and Busse, F.H., On inertial waves in a rotating fluid sphere. *J. Fluid Mech.*, 2001, 437, 103–119.

Copyright of *Geophysical & Astrophysical Fluid Dynamics* is the property of Taylor & Francis Ltd and its content may not be copied or emailed to multiple sites or posted to a listserv without the copyright holder's express written permission. However, users may print, download, or email articles for individual use.